Publications of the Astronomical Society of Australia (2025), **42**, e042, 13 pages
doi:10.1017/pasa.2025.25

CAMBRIDGE UNIVERSITY PRESS

Research Article

Brown dwarf number density in the JWST COSMOS-Web field

Amos Y.A. Chen[1], Tomotsugu Goto[1,2], Cossas K.-W. Wu[2], Chih-Teng Ling[2], Seong Jin Kim[2], Simon C.-C. Ho[3,4,5,6], Ece Kilerci[7], Yuri Uno[8], Terry Long Phan[2], Yu-Wei Lin[1], Tsung-Ching Yang[8] and Tetsuya Hashimoto[8]

[1]Department of Physics, National Tsing Hua University, Hsinchu, Taiwan, [2]Institute of Astronomy, National Tsing Hua University, Hsinchu, Taiwan, [3]Research School of Astronomy and Astrophysics, The Australian National University, Canberra, ACT, Australia, [4]Centre for Astrophysics and Supercomputing, Swinburne University of Technology, Hawthorn, VIC, Australia, [5]OzGrav: The Australian Research Council Centre of Excellence for Gravitational Wave Discovery, Hawthorn, VIC, Australia, [6]ASTRO3D: ARC Centre of Excellence for All-sky Astrophysics in 3D, Canberra, ACT, Australia, [7]Sabancı University, Faculty of Engineering and Natural Sciences, Istanbul, Turkey and [8]Department of Physics, National Chung Hsing University, Taichung, Taiwan

Abstract

Brown dwarfs are failed stars with very low mass (13–75 Jupiter mass) and an effective temperature lower than 2 500 K. Their mass range is between Jupiter and red dwarfs. Thus, they play a key role in understanding the gap in the mass function between stars and planets. However, due to their faint nature, previous searches are inevitably limited to the solar neighbourhood (20 pc). To improve our knowledge of the low mass part of the initial stellar mass function and the star formation history of the Milky Way, it is crucial to find more distant brown dwarfs. Using James Webb Space Telescope (JWST) COSMOS-Web data, this study seeks to enhance our comprehension of the physical characteristics of brown dwarfs situated at a distance of kpc scale. The exceptional sensitivity of the JWST enables the detection of brown dwarfs that are up to 100 times more distant than those discovered in the earlier all-sky infrared surveys. The large area coverage of the JWST COSMOS-Web survey allows us to find more distant brown dwarfs than earlier JWST studies with smaller area coverages. To capture prominent water absorption features around 2.7 μm, we apply two colour criteria, $\mathrm{F115W} - \mathrm{F277W} + 1 < \mathrm{F277W} - \mathrm{F444W}$ and $\mathrm{F277W} - \mathrm{F444W} > 0.9$. We then select point sources by `CLASS_STAR`, `FLUX_RADIUS`, and `SPREAD_MODEL` criteria. Faint sources are visually checked to exclude possibly extended sources. We conduct SED fitting and MCMC simulations to determine their physical properties and associated uncertainties. Our search reveals 25 T-dwarf candidates and 2 Y-dwarf candidates, more than any previous JWST brown dwarf searches. They are located from 0.3 to 4 kpc away from the Earth. The spatial number density of 900–1 050 K dwarf is $(2.0 \pm 0.9) \times 10^{-6}$ pc^{-3}, 1 050–1 200 K dwarf is $(1.2 \pm 0.7) \times 10^{-6}$ pc^{-3}, and 1 200–1 350 K dwarf is $(4.4 \pm 1.3) \times 10^{-6}$ pc^{-3}. The cumulative number count of our brown dwarf candidates is consistent with the prediction from a standard double exponential model. Three of our brown dwarf candidates were detected by HST, with transverse velocities 12 ± 5, 12 ± 4, and 17 ± 6 km s^{-1}. Along with earlier studies, the JWST has opened a new window of brown dwarf research in the Milky Way thick disk and halo.

Keywords: (stars:) brown dwarfs; methods: data analysis; infrared: stars

(Received 11 October 2024; revised 10 March 2025; accepted 14 March 2025)

1. Introduction

Brown dwarfs are very low-mass objects (13–75 Jupiter mass) (Osorio et al. 2000; Peña Ramírez et al. 2012; Martın et al. 2024) with an effective temperature lower than 2 500 K (Hainline et al. 2024b). Their mass range is between Jupiter and red dwarfs. Thus, they are vital to understanding the gap in mass function between stars and planets. Based on their spectral types, brown dwarfs are classified as L-dwarf ($T_{\rm eff} \sim$ 1 300–2 000 K), T-dwarfs ($T_{\rm eff} \sim$ 700–1 300 K), and Y-dwarfs ($T_{\rm eff} <$ 700 K) (e.g. Kirkpatrick et al. 1999, 2021; Cushing et al. 2011; Hainline et al. 2024b). However, brown dwarfs younger than 200 Myr can have late-M spectral type (Rebolo et al. 1995, 1996). L dwarfs can be brown dwarfs or not, depending on their age (Martín et al. 1998, 1999). Due to the low effective temperature, brown dwarfs are faint in optical and bright in infrared (IR). During the past decades, hundreds of brown dwarfs have been found by all-sky infrared surveys (e.g. Yamamura et al. 2009; Cushing et al. 2011; Kirkpatrick et al. 1999, 2021), whereas these brown dwarfs mainly were found near to ($\sim$ 20 pc) the Sun. Identifying more brown dwarfs at kiloparsec (kpc) distances helps investigate the mass function and extend its analysis to further reaches. This also offers a chance to comprehend the physical characteristics of distant brown dwarfs and their number density (Ryan & Reid 2016). However, owing to their low temperatures, brown dwarfs are very faint, making them difficult to detect at such distances with the previous IR space telescopes.

The revolutionary James Webb Space Telescope (JWST, Gardner et al. 2006; Kalirai 2018) is a state-of-the-art IR space telescope featuring a 6.5-m mirror (McElwain et al. 2023; Gardner et al. 2023) that offers remarkable sensitivity and spatial resolution. The utmost sensitivity of JWST enables the detection of extremely distant brown dwarfs in the galactic thick disk (e.g. Nonino et al. 2023; Wang et al. 2023; Hainline et al. 2024b), which have never been seen with previous generation space telescopes such as *AKARI* and the Hubble Space Telescope (HST).

Corresponding author: Amos Y.A. Chen; Email: yuanchen@gapp.nthu.edu.tw

Cite this article: Chen AYA, Goto T, Wu CKW, Ling CT, Kim SJ, Ho SCC, Kilerci E, Uno Y, Phan Terry Long, Lin YW, Yang TC and Hashimoto T. (2025) Brown dwarf number density in the JWST COSMOS-Web field. *Publications of the Astronomical Society of Australia* **42**, e042, 1–13. https://doi.org/10.1017/pasa.2025.25

© The Author(s), 2025. Published by Cambridge University Press on behalf of Astronomical Society of Australia. This is an Open Access article, distributed under the terms of the Creative Commons Attribution licence (https://creativecommons.org/licenses/by/4.0/), which permits unrestricted re-use, distribution and reproduction, provided the original article is properly cited.

The molecular absorption (H_2O, CH_4, NH_3, etc.) features of brown dwarfs at 1–5 μm align with the bandwidth range of NIRCam, making it well-suited for identifying brown dwarfs. Since the launch of JWST, distant brown dwarfs have been found through JWST's deep-field surveys, including the CEERS, JADES, and GOODS (e.g. Langeroodi & Jens 2023; Wang et al. 2023; Nonino et al. 2023; Hainline et al. 2024b). Therefore, expanding our search to a much larger area, such as the COSMOS-Web survey field with four NIRCam filters, greatly increases our chance of discovering even more distant brown dwarfs.

In this work, we search for brown dwarf candidates in the COSMOS-Web field and show their best-fit temperature, surface gravity, and metallicity from the Spectral Energy Distribution (SED) fitting results. By finding more distant brown dwarfs in our Milky Way, we are able to probe the initial mass function of these low-mass stars and the star formation history in our Milky Way.

This paper is structured as follows. We describe the data and filters in Section 2, candidate selection and SED fitting in Section 3, results in Section 4, discussion of transverse velocity and number density in Section 5, and conclusions in Section 5.

2. Data

2.1 Images

The JWST Cosmic Evolution Survey (COSMOS-Web) survey (Casey et al. 2023) spans 0.54 deg^2 in the COSMOS field (Scoville et al. 2007b) utilising the Near-Infrared Camera (NIRCam Rieke et al. 2023), making it the largest JWST survey field to date. The survey covered an area 18 times greater than the previous CEERS survey. Ryan & Reid (2016) estimated that there are 21.4 T0-T5 dwarfs within the COSMOS-Web field, which is seven times more than those T0-T5 dwarfs found in the CEERS field (Hainline et al. 2024b). Thus, we search for brown dwarfs in the COSMOS-Web field and anticipate discovering numerous instances.

We download the NIRCam mosaic images of the data release 0.5 (DR0.5) from the COSMOS-Web website.[a] The DR0.5 includes observations carried out in April/May 2024 (observation numbers 043-048 and 078-153), spanning a total area of 0.27 deg^2. The COSMOS-Web team (Franco et al. 2023; Casey et al. 2023) processed the raw image data using the JWST calibration pipeline v1.10.0 (Bushouse et al. 2023). The data comprised ten smaller mosaic images of rectangular tiles (A1–A10) and were covered by four NIRCam filters: F115W, F150W, F277W, and F444W. Due to a possible file collapse, F444W was missing in the A8 field, resulting in an effective area of 0.243 deg^2. This survey area is still nine times larger than the early CEERS survey.

To increase the photometric data points of our candidates, we also check the images at six shorter wavelengths from HST/Advanced Camera for Surveys (ACS) (Koekemoer et al. 2007) and SUBARU/Suprime-Cam (SC) (Taniguchi et al. 2015) and cross-match our candidates with the COSMOS2020 catalogue. We utilise the cutout images[b] of filter F814W from HST/ACS, cutout images of filters IA427, IA484, IA527, IA624, and IA709 from SUBARU/SC to scrutinise the possible detection at shorter wavelengths. 3σ detection limits of SUBARU/SC filters and 5σ detection limits of the HST/ACS filter are listed in Table 1.

[a]https://exchg.calet.org/cosmosweb-public/DR0.5/NIRCam/Apr23/.
[b]https://irsa.ipac.caltech.edu/data/COSMOS/index_cutouts.html.

Table 1. Table of the filters used in this search and their depth. The depths of SUBARU/SC filters is 3σ. The depth of the HST/ACS F814W filter and JWST/NIRCam filters are 5σ.

Survey	Filter	λ_{eff} (Å)	Depth (AB)
SUBARU/SC	IA427	4 263.5	25.8
(Taniguchi et al. 2015)	IA484	4 849.2	25.9
	IA527	5 261.1	25.7
	IA624	6 232.9	25.7
	IA709	7 073.6	25.4
HST/ACS (Scoville et al. 2007a)	F814W	8 045.5	28.6
JWST/NIRCam	F115W	11 542.61	27.45
	F150W	15 007.44	27.66
	F277W	27 617.40	28.28
	F444W	44 043.15	28.17

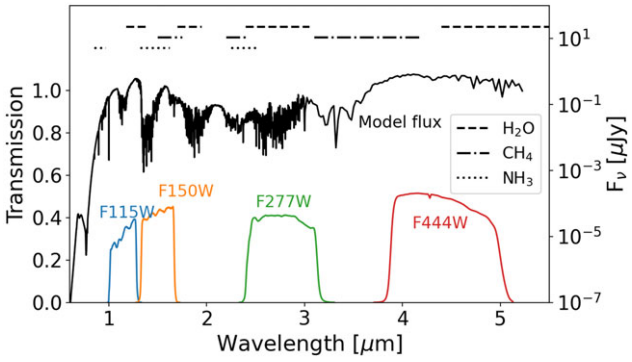


Figure 1. A brown dwarf model and transmission of NIRCam filters used in the COSMOS-Web survey. The black solid curve is the best-fit SED model for our brown dwarf candidate BD01. Coloured curves are transmission curves for four NIRCam filters. The dashed, dash-dotted, and dotted lines indicate the absorption region of H_2O, CH_4, and NH_3.

2.2 Photometry

We perform source extraction and photometry on JWST data with the photometry software SExtractor (Bertin & Arnouts 1996). The details of this process will be written in Wu et al. (in preparation). The 5σ detection limits and transmissions of four JWST/NIRCam filters are listed in Table 1 and Fig. 1.

3 Methods

3.1 Cross-match COSMOS-web catalogues

We compile a catalogue by cross-matching the catalogues of four JWST/NIRCam bands. Since brown dwarfs are brighter in the F444W band than in the F277W band, F444W is used as the detection band and cross-matched with the other three bands. We fit the separation of matched sources with the Gaussian distribution and use 5σ radii to merge F444W sources with sources from the other three bands.

5σ cross-matching radii are 0,043″, 0,070″, and 0.080″ for F444W detected sources merged with F277W, F150W, and F115W detected sources. We select brown dwarf candidates from this band-merged catalogue. There are 113 456 sources in this band-merged catalogue. During the cross-match process, 180 F444W

https://doi.org/10.1017/pasa.2025.25 Published online by Cambridge University Press

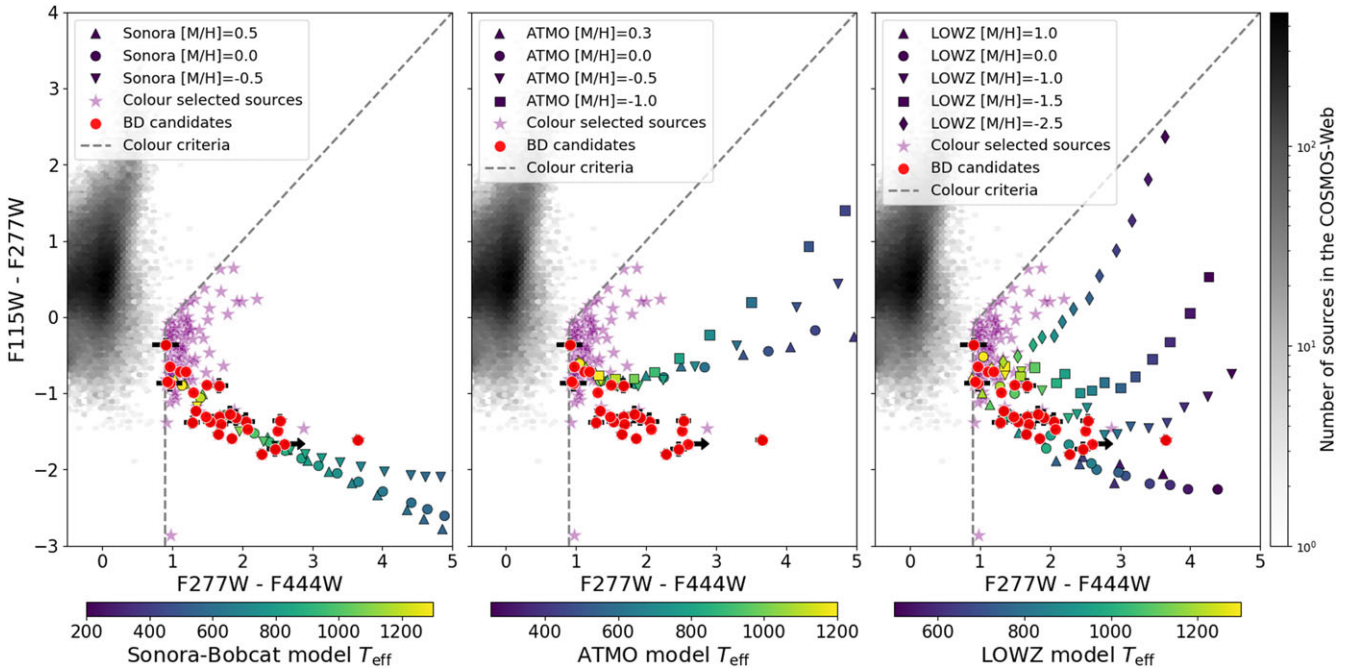


Figure 2. F277W-F444W vs F115W-F277W colour-colour plot. Grey hexagonal bins are all sources in the search area. Purple stars are sources selected by the colour criteria (Equations 1 and 2). Red circles with black error bars are 27 brown dwarf candidates. Black arrows show the non-detection in the F277W band. We plot the colours of Sonora-Bobcat, ATMO2020++, and LOWZ models in the left, middle, and right panels. Different markers represent different metallicities, and they are coloured by temperature. The surface gravity $\log g$ (cgs) is fixed at 4.5 for three models. C/O is fixed at 0.55 and $\log K_{zz}$ is fixed at 2 for LOWZ model.

detected sources matched with multiple F115W sources. We apply the same colour criteria to those 180 pairs, and one pair of sources passes through the criteria. This source was rejected because it is extended in F444W, so this multiple match does not affect our results.

3.2 Colour criteria

Brown dwarfs exhibit prominent absorption near 2.7 μm due to water and methane molecules (Marley & Robinson 2015). These objects exhibit 'V'-shaped SED and point-source morphology (Wang et al. 2023; Hainline et al. 2024b). We use two colour criteria to select these 'V'-shaped SED objects:

$$\mathrm{F115W} - \mathrm{F277W} + 1 < \mathrm{F277W} - \mathrm{F444W} \quad (1)$$

$$\mathrm{F277W} - \mathrm{F444W} > 0.9 \quad (2)$$

These criteria are designed to capture the absorption feature of brown dwarfs cooler than 1 300 K, according to three brown dwarf models: Sonora-Bobcat (Marley et al. 2021b), ATMO2020++ (Meisner et al. 2023), and LOWZ (Meisner et al. 2023). By utilising three distinct brown dwarf models, we aim to uncover diverse brown dwarfs in the thick disk and galactic halo. Distant brown dwarfs that belong to the thick disk or halo are expected to have subsolar metallicities (Hallakoun & Maoz 2021; Meisner et al. 2023). Recent spectroscopically confirmed brown dwarfs at kpc scales also show subsolar metallicities (Burgasser et al. 2024; Hainline et al. 2024a). Therefore, we include ATMO2020++ and LOWZ models, which extend the metallicity down to −1 and −2.5 dex.

In Fig. 2, we present three colour-colour plots to show the colours of three models and brown dwarf candidates in the field we used. In the plot, we fix the surface gravity $\log g$ (cgs)= 4.5 for all models and fix the carbon-to-oxygen (C/O) ratio 0.55, vertical eddy diffusion coefficient $\log K_{zz} = 2$ for LOWZ model to avoid a cluttered image. Out of 113 456 sources, 120 sources pass these colour selections.

3.3 Selecting point sources

To differentiate galaxies from stars, Wang et al. (2023) utilised the CLASS_STAR parameter from the output of the SExtractor as a selection criterion. They selected sources with CLASS_STAR > 0.9 as stars. We also apply the CLASS_STAR criteria but with a lower threshold of 0.86. We decide to lower the threshold since we find 2 moving sources that have CLASS_STAR< 0.9 in one band. BD27 is a moving source with $\mathtt{CLASS_STAR}_{\mathtt{F115W}} = 0.09$, and CLASS_STAR> 0.94 for the other three bands. It looks a little extended in F115W, so the $\mathtt{CLASS_STAR}_{\mathtt{F115W}}$ is not high. We still include this source as it is a moving source with CLASS_STAR> 0.94 in other bands. BD26 is another moving source with $\mathtt{CLASS_STAR}_{\mathtt{F277W}} = 0.86$. BD26 is not extended in F277W, and CLASS_STAR> 0.99 for the other three bands. Thus, we lower the criteria to find possible missing stars. If any band of a source meets the Equations 3–6, we remove that source.

$$\mathtt{CLASS_STAR}_{\mathtt{F115W}} < 0.86 \cap F115W < 24.5 \quad (3)$$

$$\mathtt{CLASS_STAR}_{\mathtt{F150W}} < 0.86 \cap F150W < 25 \quad (4)$$

$$\mathtt{CLASS_STAR}_{\mathtt{F277W}} < 0.86 \cap F277W < 25 \quad (5)$$

$$\mathtt{CLASS_STAR}_{\mathtt{F444W}} < 0.86 \cap F444W < 24.5 \quad (6)$$

We classify faint detections that fall outside the bimodal zone by visual inspection. Out of 120 colour-selected sources, five are rejected by these criteria. Only BD26 is affected by the lowered criteria. However, most of our sources are not bright enough to apply

https://doi.org/10.1017/pasa.2025.25 Published online by Cambridge University Press

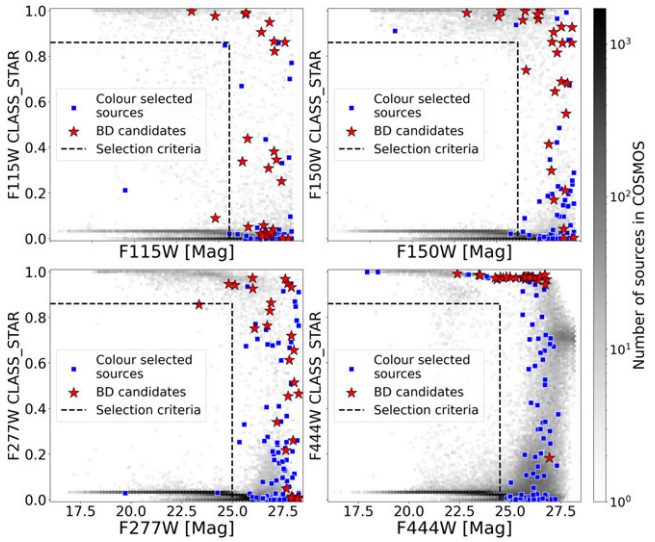


Figure 3. CLASS_STAR distribution against AB magnitude in each JWST band. Grey hexagonal bins show CLASS_STAR of all sources in the search area. Blue squares show the sources selected by colour criteria (Equations 1 and 2), which include extended sources and galaxies. Red stars are the 27 final brown dwarf candidates. Dash lines are the selection criteria.

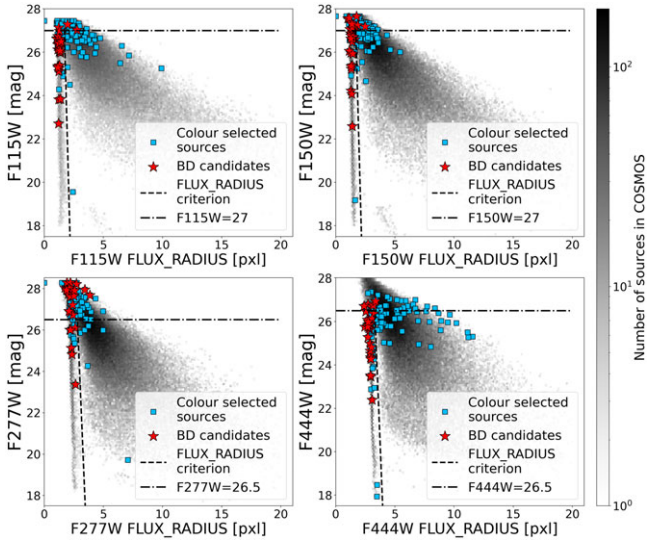


Figure 4. FLUX_RADIUS distribution against AB magnitude in each JWST band. Grey hexagonal bins show FLUX_RADIUS of all sources in the search area. The dashed line is the FLUX_RADIUS criterion for selecting point sources (Equations 7–10). The dash-dotted line is the magnitude limit to apply the FLUX_RADIUS criterion. Light blue squares show the colour-selected sources. Red stars are the final 27 brown dwarf candidates.

this method. In Fig. 3, we show the CLASS_STAR against AB magnitude distribution of colour-selected sources and all sources in the field. The 27 final brown dwarf candidates are also shown in the figure. Most colour-selected sources do not fall within the bright region where the classification is reliable. Therefore, they cannot be classified by the CLASS_STAR.

We utilise another parameter FLUX_RADIUS to establish efficient criteria. SExtractor provides a FLUX_RADIUS parameter for each source to measure its size in units of pixels. The FLUX_RADIUS-AB magnitude plot (see Fig. 4) shows a bimodality that distinguishes point sources and extended sources up to

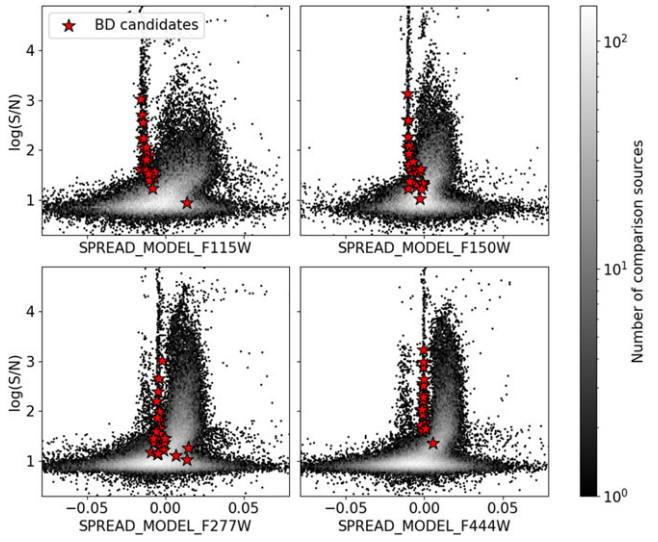


Figure 5. SPREAD_MODEL against S/N distribution for each JWST bands. The red stars are the final 27 brown dwarf candidates. The grey hexagonal bins are comparison sources.

26.5 27 magnitudes. Therefore, we can use the following equations to remove extended sources.

$$20\,\mathrm{FLUX_RADIUS}_{\mathrm{F115W}} + 61 > F115W \cap F115W < 27 \quad (7)$$

$$20\,\mathrm{FLUX_RADIUS}_{\mathrm{F150W}} + 61 > F150W \cap F150W < 27 \quad (8)$$

$$12.1\,\mathrm{FLUX_RADIUS}_{\mathrm{F277W}} + 60.4 > F277W \cap F277W < 26.5 \quad (9)$$

$$12.1\,\mathrm{FLUX_RADIUS}_{\mathrm{F444W}} + 65.4 > F444W \cap F444W < 26.5 \quad (10)$$

The unit of FLUX_RADIUS is in pixels, and the size of a pixel is 0.03″. If any band of a source meets the Equations 7–10, we remove that source. We classify faint detections that fall outside the bimodal zone by visual inspection. 72 extended sources are excluded from 115 sources. We further reject four sources that are contaminated by starlight during image inspection. There are 39 candidates in total.

Another SExtractor parameter, SPREAD_MODEL, also can be used to separate stars and galaxies (Bouy et al. 2013). SPREAD_MODEL compares the best-fitting local PSF model (representing a point source) with a slightly fuzzier model (representing a galaxy) to determine which matches the image data better. SPREAD_MODEL is close to zero for point sources, positive for extended sources (galaxies), and negative for detections smaller than the PSF, such as cosmic ray hits. We use PSFEx to extract PSF models from official PSFs,[c] then measure SPREAD_MODEL of our brown dwarf candidates and comparison sources (10% of the sources in the COSMOS-Web DR0.5 field). The SPREAD_MODEL against signal-to-noise ratio (S/N) plots are shown in Fig. 5. Although there is a clear separation between point sources and extended sources, SPREAD_MODEL of point sources at F115W, F150W, and F277W bands slightly deviate from the zero. The deviation might result from employing official PSF models instead of deriving PSF models directly from actual images. All of our brown dwarf candidates with high S/N photometry are located in the point source group, which gives us more confidence in our candidates.

[c] https://jwst-docs.stsci.edu/jwst-near-infrared-camera/nircam-performance/nircam-point-spread-functions.

https://doi.org/10.1017/pasa.2025.25 Published online by Cambridge University Press

Table 2. Observed AB magnitudes of brown dwarf candidates.

ID	R.A. (Deg)	Dec. (Deg)	F115W	F150W	F277W	F444W
BD01	150.285544	1.746714	25.36±0.02	25.98±0.03	26.85±0.04	24.346±0.007
BD02	150.235099	1.786092	27.1±0.1	27.07±0.09	28.04±0.08	26.37±0.05
BD03	150.296833	1.811298	26.46±0.06	26.71±0.07	27.82±0.09	25.29±0.01
BD04	150.175013	2.072088	23.823±0.006	24.219±0.007	25.128±0.009	23.454±0.003
BD05	150.294518	2.118124	26.12±0.04	26.87±0.07	27.92±0.07	25.64±0.02
BD06	150.078846	2.036970	26.36±0.05	26.59±0.07	27.76±0.09	26.07±0.03
BD07	150.189876	2.162042	25.12±0.02	25.24±0.02	26.01±0.02	24.517±0.008
BD08	149.817837	1.948249	26.64±0.06	26.71±0.08	28.01±0.08	26.47±0.04
BD09	149.866037	1.966471	26.20±0.05	26.76±0.06	27.74±0.07	26.08±0.02
BD10	149.876559	1.968079	26.57±0.06	27.18±0.08	27.9±0.1	25.90±0.02
BD11	149.970979	1.947989	26.62±0.06	27.56±0.09	>28.28	25.69±0.02
BD12	149.877582	2.077667	26.74±0.08	27.36±0.09	28.1±0.1	26.14±0.04
BD13	149.793271	2.150532	25.98±0.04	26.48±0.06	27.21±0.07	25.87±0.03
BD14	149.867104	2.192126	26.98±0.08	27.3±0.1	>28.28	26.80±0.05
BD15	149.820286	2.245290	25.26±0.04	26.06±0.03	26.73±0.04	24.651±0.009
BD16	149.780389	2.282369	26.62±0.08	27.6±0.1	28.00±0.08	26.71±0.04
BD17	150.071463	1.827356	26.02±0.04	26.62±0.05	27.61±0.06	25.76±0.02
BD18	150.126952	1.814842	26.31±0.05	27.06±0.07	27.92±0.07	24.267±0.006
BD19	150.152366	1.846883	26.41±0.06	27.12±0.08	27.7±0.1	25.85±0.02
BD20	150.191908	1.883924	26.48±0.07	27.3±0.1	28.22±0.09	25.75±0.02
BD21	150.282550	1.877380	27.3±0.2	27.2±0.2	27.65±0.07	26.74±0.06
BD22	150.170275	1.997987	27.0±0.2	27.7±0.1	27.90±0.08	26.94±0.07
BD23	150.305087	2.049419	25.39±0.03	25.39±0.02	26.10±0.03	24.99±0.01
BD24	149.882442	1.989569	25.29±0.02	25.35±0.02	26.00±0.02	24.81±0.01
BD25	150.121254	1.871543	26.07±0.04	25.93±0.03	26.91±0.04	25.98±0.03
BD26	150.247519	1.810540	22.706±0.003	22.583±0.002	23.355±0.003	22.389±0.001
BD27	149.947777	2.047444	23.836±0.008	24.078±0.007	24.819±0.007	23.514±0.003

3.4 SED fitting

As mentioned in Langeroodi & Jens (2023), the colour of brown dwarfs resembles that of active galactic nuclei (AGNs). There may be AGN contaminants among our colour-selected candidates. To confirm the brown dwarf nature of these candidates and accurately determine their physical properties, we perform SED fitting using the software LePhare (Arnouts et al. 1999; Ilbert et al. 2006). LePhare includes three categories of templates: galaxy, quasi-stellar object (QSO), and stars. For galaxies, we adopt the CWW_Kinney spectra (Coleman, Wu, &Weedman 1980; Calzetti, Kinney, &Storchi-Bergmann 1994) and include all QSO spectra (Rowan-Robinson et al. 2008; Netzer et al. 2007; Silva et al. 1998), encompassing both observed and synthetic spectra. For stellar SEDs, in addition to the library provided in LePhare (Pickles 1998; Chabrier et al. 2000; Hamuy et al. 1994), we manually incorporated the Sonora-Bobcat (Marley & Robinson 2015), ATMO2020++ (Meisner et al. 2023), and LOWZ(Meisner et al. 2023) brown dwarf models. We fit each source three times with these brown dwarf models separately.

Sonora-Bobcat model provides brown dwarf SEDs with effective temperature ($T_{\rm eff}$) 200 K $\leq T_{\rm eff} \leq$ 2 400 K, gravity (g) 3 $\leq \log g$ (cgs) $\leq$ 5.5 and three metallicities ([M/H]) $= -0.5$, 0.0, and 0.5. The temperature steps are 25, 50, and 100 K, depending on the temperature. The surface gravity $\log g$ step is 0.25. The model spectra cover from 0.66 to 5.26 μm. We use one specific ATMO2020++ model (Leggett et al. 2021) that provides the sub-solar metallicity parameter down to −1.0 dex to find metal-poor brown dwarfs. This model provides SEDs with 250 K $\leq T_{\rm eff} \leq$ 1 200 K, 2.5 $\leq \log g$ (cgs) $\leq$ 5.5, and four metallicity options: −1.0, −0.5, 0.0, and 0.3. The temperature steps are 25, 50, and 100 K, depending on the temperature. The surface gravity $\log g$ step is 0.5. LOWZ model provides SEDs with 500 K $\leq T_{\rm eff} \leq$ 1 600 K with temperature steps 50 and 100 K, five $\log g$ (cgs) options: 3.5, 4.0, 4.5, 5.0, and 5.25, three carbon-to-oxygen (C/O) ratio: 0.1, 0.55, and 0.85, three vertical eddy diffusion coefficient $\log K_{zz}$ (cgs): −1.0, 2.0, 10.0, and $-2.5 \leq$ [M/H] $\leq$ 1.0 with step sizes 0.25 and 0.5.

To check the proper motion and increase photometric data points, we cross-match our brown dwarf candidates with the COSMOS2020 catalogue (Weaver et al. 2022). Considering the potential proper motion of these stars, we choose a wide cross-match radius of 1.5 arcsec based on the result of Hainline et al. (2024b). The average time gap between the HST COSMOS and JWST images is 20 yr. By scaling the proper motion of the brown dwarf candidates using the highest proper motion from Hainline et al. (2024b) (0.75″ over 10 yr), we estimate the largest proper

https://doi.org/10.1017/pasa.2025.25 Published online by Cambridge University Press

motion to be 1.5″. This corresponds to a velocity of 178 km/s at 500 pc.

4. Results

Among 120 colour-selected sources, CLASS_STAR criteria rejected 5 of them, and 72 were rejected by the FLUX_RADIUS criteria (Section 3.2). No sources were rejected by SPREAD_MODEL. 4 out of the remaining 43 sources were contaminated with nearby starlight. 17 out of 39 sources matched with COSMOS2020 sources. Only one COSMOS2020 source that matched with BD26 was labeled as a star. Although 16 matched COSMOS2020 sources were labelled as galaxies, we found 14 of them were only detected in a few IR bands and had no detections in optical. Only 2 matched COSMOS2020 sources were detected by SUBARU/SC filters, which are definitely galaxies. We removed those 2 brown dwarf candidates that matched with these two galaxies. Considering that brown dwarf models were published after 2021, we believe those 14 COSMOS2020 sources are misclassified as galaxies.

27 out of 37 sources best fit with 3 brown dwarf models simultaneously, showing a large discrepancy with galaxy SEDs. 8 sources have the smallest chi-square (χ^2) with neither of the three models, so they are classified as galaxies and removed. 2 sources best fit with one or two brown dwarf models. As they were only detected in 3 bands and did not best fit with all brown dwarf models, we removed these two candidates. Three moving sources, BD04, BD26, and BD27, were detected clearly by HST/ACS F814W and 4 UltraVISTA bands. Their angular separation and transverse velocities are discussed in Section 5.3. These three brown dwarfs have 9 band detections, so we use 9 photometry bands in the SED fitting. There are 27 brown dwarf candidates in total. Their coordinates and colours are shown in Table 2. All fitting results are shown in Figs. 6–7.

To estimate the uncertainty of the fitting parameters and the estimated distance, we perform a Markov chain Monte Carlo (MCMC) analysis with PYTHON package EMCEE. We linearly interpolate the model magnitude table with step size 5 K for $T_{\rm eff}$, 0.1 for $\log g$, and 0.1 for Z. LOWZ's C/O and $\log K_{zz}$ parameter are not interpolated to save the computation time. In addition, the observed photometry was fitted to the interpolated models, and the likelihood function was maximised. We set the prior probability uniformly within the three models' parameter space and zero beyond it. In addition to the three (five) parameters for Sonora-Bobcat and ATMO2020++ (LOWZ), a new parameter, distance (D), is included in the MCMC analysis. Since the authors of the Sonora-Bobcat model provide the magnitude of brown dwarf models at 10 pc for JWST filters (Marley et al. 2021a), we are able to fit the observed magnitude to the 10 pc model magnitude and derive their distances. Distance can also be directly derived from ATMO2020++ fitting as the SEDs are provided at 10 pc. LOWZ provides SEDs with surface fluxes, so we fit the scale factor $\alpha = (R/D)^2$ to the observed flux densities. R is the radius of the source, and we assume a common radius of one Jupiter radius (Burgasser et al. 2024; Hainline et al. 2024a) for 27 brown dwarf candidates to derive D. We use 120 walkers and 5 000 steps in the MCMC analysis for 24 sources that were not detected by HST. For those three brightest brown dwarf candidates that have one HST, four UltraVISTA, and four JWST photometry, we run another MCMC fitting with 9ninephotometry bands. In this MCMC fitting, we use 120 walkers and 6 000 steps. The MCMC results for each source are listed in Tables 3–5. Sonora-Bobcat model fitting results peak at one single solution for all sources, while ATMO2020++ and LOWZ's results have multiple solutions for some candidates. MCMC walkers converge to several peaks, and this degeneracy cannot be resolved by MCMC fitting through doubling the steps. Among the multi-solutions of one brown dwarf candidate, we list one solution with more walkers that converge to it and mark it with a footnote.

To identify the type of brown dwarf candidates and compare their number density, we perform another SED fitting to our brown dwarf candidates with spectra of L-dwarf IR standards (Reid et al. 2008), T-dwarf IR standards (Burgasser et al. 2006), and the NIRSpec PRISM spectrum of a Y0-dwarf WISEPC J205628.90+145953.3 (Beiler et al. 2024). The spectra for the L and T dwarf standards are taken from the SpeX library,[d] while the spectrum for the Y0-dwarf is obtained from JWST observations.[e] Since spectra of L and T type brown dwarfs range from 0.66 to 2.56 μm, we only use 0.66 to 2.56 μm part of the Y0-dwarf spectrum to have a proper SED fitting. It is important to note that only two photometric data points are within this spectral range. Therefore, additional observations are needed to determine the spectral type of these brown dwarf candidates more precisely. The best-fit type of these brown dwarf candidates is listed in Table 3. We find five T2, three T3, four T4, eight T5, four T7, one T8, and two Y0 dwarf candidates in our survey field.

Our study heralds a new chapter in the exploration of brown dwarfs. The ultimate sensitivity of JWST enables the discovery of brown dwarfs situated several kpc from Earth.

5. Discussion

5.1 Colour degeneracies

In the MCMC fitting, Sonora-Bobcat and LOWZ converge to similar $T_{\rm eff}$. Due to the model's temperature grid limit, ATMO2020++ models converge to similar $T_{\rm eff}$ for $T_{\rm eff} < 1\,200$ K. Sonora-Bobcat model tends to fit a higher $T_{\rm eff}$ than ATMO2020++ and LOWZ, which results in a larger distance. In addition to Sonora-Bobcat, ATMO2020++ and LOWZ both show multiple solutions to some sources (see Tables 3–5, they are marked with footnotes). This may be due to the small number of filters, or because the true solutions are beyond the model's parameter ranges. We note that one of the multi-solutions, the ATMO2020++ MCMC fitting result of BD02, shows a very low $\log g \sim 2.5$. Such low log g values are atypical for field brown dwarfs, which are older and more compact, generally having surface gravities of $\log g \sim 4.5$ (Allers & Liu 2013; Gizis et al. 2015). Instead, $\log g \sim 2.5$ is more commonly associated with young, low-mass objects (Allers & Liu 2013; Martin et al. 2017), which are not likely to be found in the field. For $T_{\rm eff} \gtrapprox 1\,300$ K candidates, LOWZ's MCMC fittings often converge to high metallicities ($\simeq 1$ dex.) and low metallicities ($\simeq -2$ dex.) solutions. We cannot distinguish these solutions with only four JWST filters at 1.1, 1.5, 2.7, and 4.4 μm. Although the spectrum shape differs, fluxes are similar after convolving with JWST filters. The most significant difference is at 2 μm. We fix the C/O = 0.55 and $\log K_{zz} = 2$, then compare LOWZ models with $T_{\rm eff} = 1\,300$ K and all $\log g$. After convolving with UltraVISTA's Ks filter (2.1 μm), we find the colour difference of F150W-Ks of low metallicity solution is $\simeq 2$ magnitude smaller than the high metallicity solution.

[d] https://cass.ucsd.edu/ajb/browndwarfs/spexprism/library.html.
[e] https://archive.stsci.edu/doi/resolve/resolve.html?doi=10.17909/ntwg-k441.

https://doi.org/10.1017/pasa.2025.25 Published online by Cambridge University Press

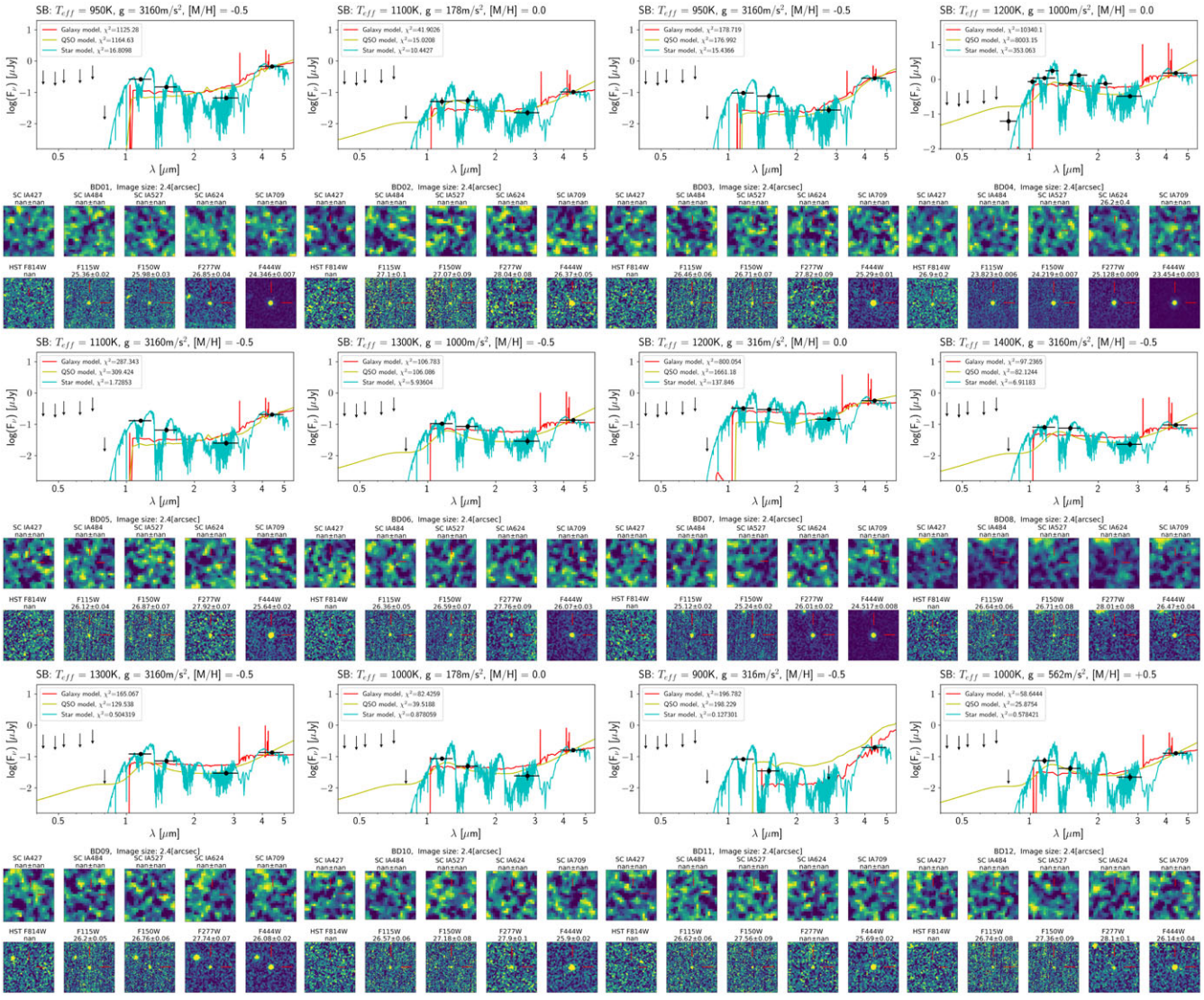


Figure 6. SED fitting results and images of brown dwarf candidates. The title of each figure shows the temperature, surface gravity, and metallicity of the best-fit Sonora-Bobcat model. Black dots with error bars are the photometric data points, and arrows represent the upper limit of that band. The red line is the spectrum of the best-fit galaxy model, the yellow line is the best-fit QSO model, and the cyan line is the best-fit Sonora-Bobcat template. Parameters of the best-fit brown dwarf model are shown at the top of the figure. The χ^2 of each template is listed in the caption. The lower panel is the cutout images of SUBARU/SC, HST/ACS, and JWST/NIRCam at the brown dwarf position. The image size is $2.4'' \times 2.4''$. The number in each cutout image represents the measured photometry along with its error expressed in AB magnitude units. Nan represents no detection or is lower than the detection limit in that filter. The F277W photometry results of BD11 and BD14 are fainter than the F277W 5σ detection limit, so they are labelled as no detection in the F277W band.

Therefore, JWST/NIRCam F200W or F210M photometry is necessary for constraining the metallicity of brown dwarfs.

5.2 Metallicity

We expect to find sub-solar metallicity brown dwarfs at kpc scales (see Section 3.2). However, LOWZ often gives both low metallicity and high metallicity solutions for every low metallicity candidate. Sonora-Bobcat only gives one solution to each source, but the metallicity just ranges from -0.5 to 0.5 dex. As we discussed in Section 5.1, we need observations at 2 μm to constrain the metallicities of these brown dwarf candidates. Previous studies of metal-poor brown dwarf candidates have shown strong colour variations with chemical composition (Lodieu et al. 2022; Meisner et al. 2023; Burgasser et al. 2024; Zhang et al. 2023). This might also complicate accurately determining the metallicities.

5.3 Transverse velocity

Three brown dwarf candidates, BD04, BD26, and BD27, were detected in both HST and JWST. They are the three brightest candidates in the F115W band. Images from the HST were captured between July 2003 and June 2005, resulting in an average interval of 19 yr prior to the JWST's images in 2023. We use SExtractor to extract positions of brown dwarf candidates' HST detections. The astrometry accuracy of our JWST photometry is 0.038″ (Wu et al. in preparation), which is adopted for both JWST and HST positions. We calculate the errors of the proper motions, which

https://doi.org/10.1017/pasa.2025.25 Published online by Cambridge University Press



Figure 7. SED fitting results and images of brown dwarf candidates (continued from Fig. 6).

https://doi.org/10.1017/pasa.2025.25 Published online by Cambridge University Press

Table 3. Physical properties derived from MCMC fitting and spectral-type fitting results of the brown dwarf candidates. We show the temperature, surface gravity, and metallicity of brown dwarf candidates for each brown dwarf model. The left column of each parameter is the median of the distribution. The upper-/lower error stands for the 16th and 84th percentiles of the distribution, respectively. The uncertainties that are smaller than the grid size are shown as the grid size of that parameter. The right column of each parameter is the peak value of the distribution. The unit of temperature is kelvin, the unit of gravity is cm s^{-2}, metallicity is relative to that of the Sun, and the candidate's distance from Earth is in pc. The last column shows the best-fit spectral type of each brown dwarf candidate.

ID	Model	$T_{\rm eff}$ (K)		log g (cgs)		Z ([M/H])		C/O		log K_{zz} (cgs)		D (pc)		Type
BD01	Sonora-Bobcat	958^{+6}_{-7}	959	$5.5^{+0.1}_{-0.1}$	5.5	$-0.5^{+0.1}_{-0.1}$	−0.5					491^{+15}_{-5}	489	T5
	ATMO2020++	813^{+5}_{-5}	812	$5.5^{+0.1}_{-0.1}$	5.6	$0.3^{+0.1}_{-0.1}$	0.3					439^{+3}_{-3}	438	
	LOWZ	869^{+30}_{-24}	861	$4.1^{+0.4}_{-0.3}$	4.1	$-0.7^{+0.1}_{-0.1}$	−0.7	$0.7^{+0.3}_{0.3}$	0.8	$1.5^{+3.2}_{3.0}$	0.2	550^{+43}_{-31}	531	
BD02	Sonora-Bobcat	$1\,195^{+40}_{-46}$	1 208	$4.7^{+0.4}_{-0.4}$	4.8	$-0.1^{+0.3}_{-0.3}$	0.0					$2\,051^{+349}_{-280}$	1 985	T2
	ATMO2020++[a]	1044^{+44}_{-42}	1 047	$2.5^{+0.2}_{-0.1}$	2.4	$-0.8^{+0.2}_{-0.2}$	−0.9					$1,538^{+133}_{-124}$	1 531	
	LOWZ	$1\,208^{+71}_{-91}$	1 238	$4.6^{+0.5}_{-0.5}$	4.9	$-0.8^{+0.4}_{-0.5}$	−0.8	$0.3^{+0.3}_{0.3}$	0.1	$5.1^{+4.0}_{4.1}$	6.1	$2\,168^{+213}_{-293}$	2 162	
BD03	Sonora-Bobcat	947^{+16}_{-20}	944	$5.4^{+0.1}_{-0.3}$	5.5	$-0.4^{+0.2}_{-0.1}$	−0.5					770^{+76}_{-31}	762	T4
	ATMO2020++[a]	886^{+35}_{-39}	884	$5.5^{+0.1}_{-0.1}$	5.6	$-0.0^{+0.2}_{-0.2}$	−0.0					827^{+69}_{-82}	830	
	LOWZ	935^{+38}_{-59}	946	$4.5^{+0.5}_{-0.7}$	5.0	$-1.0^{+0.2}_{-0.2}$	−1.1	$0.3^{+0.3}_{0.3}$	0.2	$5.2^{+4.0}_{4.4}$	9.4	968^{+82}_{-125}	1 042	
BD04	Sonora-Bobcat	$1\,227^{+6}_{-12}$	1 228	$5.2^{+0.1}_{-0.1}$	5.2	$-0.0^{+0.1}_{-0.1}$	−0.0					539^{+5}_{-11}	540	T5
	ATMO2020++	1128^{+2}_{-2}	1 128	$5.5^{+0.1}_{-0.1}$	5.5	$-0.0^{+0.1}_{-0.1}$	−0.0					443^{+1}_{-1}	443	
	LOWZ	1049^{+2}_{-2}	1 049	$4.5^{+0.1}_{-0.1}$	4.5	$0.1^{+0.1}_{-0.1}$	0.1	$0.5^{+0.3}_{0.3}$	0.7	$3.2^{+3.0}_{3.0}$	2.8	$417.8^{+0.9}_{-0.8}$	418.4	

[a] Exist multiple MCMC solutions. We list the one with more walkers, which means a higher probability.

are added in quadrature in the standard way. The proper motion (μ) in R.A. direction (μ_{ra}) and Dec. direction (μ_{dec}) for three candidates is:

$$\begin{aligned}
&\text{BD04: } \mu = 0.10'' \pm 0.038'' \\
&(\mu_{ra}, \mu_{dec}) = (0.00'' \pm 0.038'', -0.1'' \pm 0.038'') \\
&\text{BD26: } \mu = 0.11'' \pm 0.038'' \\
&(\mu_{ra}, \mu_{dec}) = (0.11'' \pm 0.038'', 0.02'' \pm 0.038'') \\
&\text{BD27: } \mu = 0.11'' \pm 0.038'' \\
&(\mu_{ra}, \mu_{dec}) = (-0.09'' \pm 0.038'', -0.07'' \pm 0.038'')
\end{aligned}$$

The one-year proper motion for each candidate is: $0.005'' \pm 0.002''$, $0.006'' \pm 0.002''$, $0.006'' \pm 0.002''$ for BD04, BD26, and BD27, respectively. Transverse velocities can be calculated by this equation $v_T = 4.74\,\mu D$, where v_T is the transverse velocity in km s^{-1}, μ is proper motion in arcsec $year^{-1}$, and D is the distance in pc. Adopting the distances and uncertainties derived from Sonora-Bobcat's MCMC fitting results, we derived the transverse velocities for each candidate: 12 ± 5, 12 ± 4, and 17 ± 6 km s^{-1} for BD04, BD26, and BD27, respectively. The brown dwarfs at 20 pc have tangential velocities peak at 20 km s^{-1} (Kirkpatrick et al. 2021), which is larger than our candidates. The small transverse velocities imply they are thin disk populations.

5.4 Number density

Ryan & Reid (2016) predicted the number density of T0–T5 dwarf in the COSMOS-Web field based on the brown dwarf luminosity function from Cruz et al. (2007), Bochanski et al. (2010), Metchev et al. (2008). They assumed the double exponential model for the spatial distribution of brown dwarfs and derived the predicted number count by integrating the number density and luminosity function. The uncertainty of the number count is not provided; therefore, we directly adopt the errors of the T0–T5 dwarfs' luminosity function as the number count error. Given the F115W 5σ detection limit 27.45, the expected number is 0.015 ± 0.009 T0–T5 dwarfs per $arcmin^2$, which is 13.1 ± 7.9 T0–T5 dwarfs in our 0.243 deg^2 searching area. If we adopt the spectral fitting results and assume Poisson distribution, the total number of T0–T5 dwarfs will be 20 ± 4.5. We also show the cumulative number count histogram in the upper panel of Fig. 8.

Here, we present another method to compare our results with those of the nearby observation and the model. We calculate the number densities of brown dwarf candidates in 3 effective temperature bins, 900–1 050, 1 050–1 200, and 1 200–1 350 K. There are 5 ± 2.2 dwarfs in $T_{\rm eff}$ range 900–1 050 K, 3 ± 1.7 dwarfs in $T_{\rm eff}$ range 1 050–1 200 K, and 11 ± 4.3 dwarfs in $T_{\rm eff}$ range 1 200–1 350 K. Next, we estimate the search volume to calculate the density. Since only the Sonora-Bobcat model does not have multiple solutions in MCMC fitting, we only adopt SEDs and the distances derived from this model. We use $T_{\rm eff} = 1\,300$ K Sonora-Bobcat model to calculate detection limits for our search. To match the colour criterion Equation (2), the 5σ detection limit of F227W= 28.28 implies the magnitude limit of F444W to find a brown dwarf is 27.38. We convert the F444W magnitude limit to the search limits of the 1 300 K model, which is 4 670 pc. The number densities are: $(2.0 \pm 0.9) \times 10^{-6}$ pc^{-3} for 900–1 050 K dwarf, $(1.2 \pm 0.7) \times 10^{-6}$ pc^{-3} for 1 050–1 200 K dwarf, and $(4.4 \pm 1.3) \times 10^{-6}$ pc^{-3} for 1 200–1 350 K dwarf. The number densities of brown dwarfs measured by Kirkpatrick et al. (2021) at 20 pc are: $(1.72 \pm 0.30) \times 10^{-3}$ pc^{-3} for 900–1 050 K dwarf, $(1.11 \pm 0.25) \times 10^{-3}$ pc^{-3} for 1 050–1 200 K dwarf, and $(1.95 \pm 0.30) \times 10^{-3}$ pc^{-3} for 1 200–1 350 K dwarf. The distribution of brown dwarfs is not uniform among the Milky Way, so densities by Kirkpatrick et al. (2021) are 3 orders of magnitude higher than those in this work.

To give a reasonable comparison, we replace the number densities that Ryan & Reid (2016) used with Kirkpatrick et al. (2021)'s densities. T0–T5 brown dwarfs have a $T_{\rm eff}$ range similar to 900–1 350 K (Kirkpatrick et al. 2021, Figure 22(b)), so we scale the T0–T5 number density with 900–1 350 K number density to get a cumulative number count for 900–1 350 K brown dwarfs. T0–T5 number density is derived by integrating Ryan & Reid (2016)'s brown dwarf luminosity function in the T0–T5 range. By scaling

https://doi.org/10.1017/pasa.2025.25 Published online by Cambridge University Press

Table 4. Physical properties derived from MCMC fitting. (Continued from Table 3)

ID	Model	$T_{\rm eff}$ (K)		log g (cgs)		Z ([M/H])		C/O		log K_{zz} (cgs)		D (pc)		Type
BD05	Sonora-Bobcat	$1\,074^{+24}_{-26}$	1 072	$5.4^{+0.1}_{-0.3}$	5.5	$-0.1^{+0.3}_{-0.3}$	−0.0					$1\,026^{+111}_{-87}$	1 025	T7
	ATMO2020++ [a]	920^{+19}_{-16}	915	$3.0^{+0.1}_{-0.1}$	3.0	$-1.0^{+0.1}_{-0.1}$	−1.0					908^{+32}_{-28}	898	
	LOWZ	883^{+62}_{-101}	915	$4.7^{+0.3}_{-0.5}$	4.9	$0.1^{+0.3}_{-0.3}$	0.1	$0.6^{+0.3}_{0.3}$	0.5	$4.5^{+4.7}_{4.0}$	0.2	904^{+123}_{-234}	978	
BD06	Sonora-Bobcat	$1\,286^{+33}_{-37}$	1 288	$5.2^{+0.2}_{-0.3}$	5.3	$-0.2^{+0.4}_{-0.3}$	−0.5					$1\,639^{+276}_{-202}$	1 500	T4
	ATMO2020++	$1\,152^{+32}_{-47}$	1 165	$5.5^{+0.1}_{-0.1}$	5.6	$0.1^{+0.2}_{-0.1}$	0.1					$1\,487^{+91}_{-126}$	1 505	
	LOWZ[a]	$1\,110^{+182}_{-101}$	1 060	$4.9^{+0.3}_{-0.6}$	5.3	$0.4^{+0.3}_{-0.3}$	0.3	$0.5^{+0.3}_{0.3}$	0.5	$7.4^{+3.0}_{4.9}$	8.1	$1\,437^{+334}_{-316}$	1 352	
BD07	Sonora-Bobcat	$1\,214^{+8}_{-10}$	1 212	$4.5^{+0.1}_{-0.1}$	4.5	$0.0^{+0.1}_{-0.1}$	0.0					932^{+21}_{-24}	922	T3
	ATMO2020++	$1\,161^{+15}_{-3}$	1 158	$5.2^{+0.1}_{-0.1}$	5.2	$-0.2^{+0.1}_{-0.1}$	−0.2					783^{+27}_{-4}	782	
	LOWZ[a]	$1\,123^{+24}_{-30}$	1 115	$4.3^{+0.1}_{-0.1}$	4.2	$-0.3^{+0.1}_{-0.3}$	−0.3	$0.6^{+0.3}_{0.3}$	0.6	$3.9^{+3.6}_{3.0}$	4.8	782^{+37}_{-38}	762	
BD08	Sonora-Bobcat	$1\,405^{+32}_{-33}$	1 405	$5.4^{+0.2}_{-0.2}$	5.6	$-0.5^{+0.2}_{-0.1}$	−0.5					$2\,140^{+199}_{-147}$	2 088	T3
	ATMO2020++	$1\,182^{+19}_{-29}$	1 198	$5.5^{+0.1}_{-0.1}$	5.5	$0.3^{+0.1}_{-0.1}$	0.3					1769^{+58}_{-85}	1 812	
	LOWZ[a]	1214^{+162}_{-73}	1 226	$5.0^{+0.2}_{-0.4}$	5.2	$0.6^{+0.1}_{-0.2}$	0.8	$0.5^{+0.3}_{0.3}$	0.7	$8.4^{+3.0}_{3.0}$	8.8	$1\,824^{+457}_{-219}$	1 862	
BD09	Sonora-Bobcat	$1\,299^{+23}_{-24}$	1302	$5.5^{+0.1}_{-0.2}$	5.5	$-0.4^{+0.3}_{-0.1}$	−0.6					$1\,559^{+124}_{-84}$	1 538	T5
	ATMO2020++	$1\,082^{+21}_{-19}$	1 079	$5.5^{+0.1}_{-0.1}$	5.6	$0.3^{+0.1}_{-0.1}$	0.3					$1\,295^{+54}_{-40}$	1 295	
	LOWZ[a]	$1\,092^{+183}_{-86}$	1 272	$5.0^{+0.2}_{-0.3}$	5.2	$0.8^{+0.3}_{-0.4}$	1.1	$0.3^{+0.3}_{0.3}$	0.1	$3.5^{+3.0}_{3.0}$	2.8	$1\,465^{+208}_{-230}$	1 645	
BD10	Sonora-Bobcat	$1\,023^{+26}_{-25}$	1 028	$4.4^{+0.5}_{-0.5}$	4.5	$-0.1^{+0.4}_{-0.3}$	−0.6					$1\,530^{+208}_{-233}$	1 560	T5
	ATMO2020++	960^{+64}_{-58}	940	$5.4^{+0.1}_{-0.2}$	5.6	$0.1^{+0.2}_{-0.3}$	−0.0					$1\,126^{+167}_{-141}$	984	
	LOWZ	918^{+64}_{-89}	939	$4.0^{+0.6}_{-0.4}$	3.6	$-0.2^{+0.5}_{-0.3}$	−0.4	$0.6^{+0.3}_{0.3}$	0.8	$3.3^{+3.9}_{3.3}$	0.2	1105^{+141}_{-211}	1 175	
BD11	Sonora-Bobcat	874^{+26}_{-25}	874	$4.0^{+0.9}_{-0.7}$	3.2	$-0.0^{+0.4}_{-0.4}$	0.1					1224^{+174}_{-240}	1 312	Y0
	ATMO2020++	765^{+64}_{-41}	750	$3.7^{+0.4}_{-0.3}$	3.7	$-0.3^{+0.4}_{-0.4}$	−0.5					668^{+145}_{-81}	620	
	LOWZ	759^{+52}_{-65}	762	$4.5^{+0.5}_{-0.7}$	5.2	$-0.0^{+0.5}_{-0.3}$	−0.2	$0.5^{+0.3}_{0.3}$	0.6	$2.5^{+3.0}_{3.0}$	0.2	784^{+119}_{-152}	818	
BD12	Sonora-Bobcat	$1\,056^{+32}_{-32}$	1 056	$4.4^{+0.5}_{-0.4}$	4.5	$-0.1^{+0.4}_{-0.3}$	−0.5					1761^{+228}_{-271}	1 842	T5
	ATMO2020++	982^{+65}_{-62}	969	$5.4^{+0.1}_{-0.2}$	5.6	$0.0^{+0.2}_{-0.3}$	−0.0					$1\,299^{+196}_{-175}$	1 158	
	LOWZ	929^{+91}_{-94}	915	$3.9^{+0.5}_{-0.3}$	3.6	$-0.1^{+0.7}_{-0.4}$	−0.3	$0.5^{+0.3}_{0.3}$	0.8	$3.7^{+4.6}_{3.6}$	−0.5	$1\,220^{+202}_{-245}$	1 230	
BD13	Sonora-Bobcat	$1\,328^{+32}_{-39}$	1 336	$5.2^{+0.3}_{-0.4}$	5.3	$-0.1^{+0.5}_{-0.3}$	−0.5					$1\,548^{+297}_{-208}$	1 525	T5
	ATMO2020++	$1\,140^{+40}_{-29}$	1 138	$5.5^{+0.1}_{-0.1}$	5.5	$0.3^{+0.1}_{-0.1}$	0.3					$1\,260^{+97}_{-58}$	1 238	
	LOWZ[a]	1438^{+29}_{-28}	1 435	$3.5^{+0.1}_{-0.1}$	3.4	$-2.2^{+0.2}_{-0.2}$	−2.2	$0.2^{+0.3}_{0.3}$	0.1	$3.0^{+3.0}_{3.0}$	2.2	$2\,058^{+84}_{-81}$	2 078	
BD14	Sonora-Bobcat	$1\,434^{+89}_{-76}$	1 391	$4.0^{+0.8}_{-0.6}$	3.8	$-0.0^{+0.4}_{-0.4}$	−0.5					$4\,077^{+1\,171}_{-1\,143}$	4 202	T4
	ATMO2020++	$1\,179^{+22}_{-37}$	1 204	$5.2^{+0.3}_{-0.2}$	5.1	$0.2^{+0.1}_{-0.2}$	0.3					$2\,037^{+82}_{-121}$	2 072	
	LOWZ[a]	1458^{+71}_{-60}	1 465	$3.8^{+0.5}_{-0.3}$	3.4	$-2.1^{+0.5}_{-0.3}$	−2.4	$0.2^{+0.3}_{0.3}$	0.2	$3.9^{+4.5}_{3.5}$	−0.5	$3\,213^{+258}_{-230}$	3 175	
BD15	Sonora-Bobcat	$1\,012^{+13}_{-25}$	1 015	$4.3^{+0.4}_{-0.3}$	4.1	$-0.2^{+0.6}_{-0.3}$	−0.5					886^{+72}_{-151}	962	T7
	ATMO2020++ [a]	803^{+7}_{-5}	805	$3.0^{+0.1}_{-0.1}$	3.0	$-0.5^{+0.1}_{-0.1}$	−0.5					438^{+7}_{-4}	438	
	LOWZ	871^{+54}_{-45}	877	$3.6^{+0.3}_{-0.2}$	3.4	$-0.1^{+0.2}_{-0.1}$	−0.2	$0.6^{+0.3}_{0.3}$	0.7	$2.8^{+3.0}_{3.0}$	0.9	564^{+70}_{-60}	562	

Ryan & Reid (2016)'s result with Kirkpatrick et al. (2021)'s measurement, we plot the cumulative number count histogram of our 900–1 350 K brown dwarf candidates with the scaled double exponential model in the lower panel of Fig. 8. The brown dwarf candidates in the histogram are selected based on the peak $T_{\rm eff}$ value from Sonora-Bobcat's MCMC fitting results. We find the temperature-based selections are more consistent with the model than the spectral type-based selections. The discrepancy in the cumulative number count of T0–T5 from the model might come from the inaccurate spectral type fitting, in which we only use two photometry data points for most of the sources. Four photometry information are used to fit the $T_{\rm eff}$, so the 900–1 350 K cumulative number count is more precise. The lower panel of Fig. 8 also shows that our brown dwarf distribution is consistent with the double exponential model. However, both comparisons we present in Fig. 8 suffer from small number statistics. Larger survey data are needed to confirm this result.

6. Conclusion

Using the JWST COSMOS-Web DR0.5 field (0.243 deg^2), we search for distant, faint brown dwarf candidates. To capture H_2O absorption around 2.7 μm, we select point sources (`CLASS_STAR`, `FLUX_RADIUS`, and `SPREAD_MODEL` criteria, Equations 3–10) with colours F115W − F277W + 1 < F277W − F444W and F277W-F444W>0.9 as brown dwarf candidates. We perform SED fitting and MCMC simulations with three brown dwarf models to determine their physical properties and associated uncertainties. Our main findings are:

https://doi.org/10.1017/pasa.2025.25 Published online by Cambridge University Press

Table 5. Physical properties derived from MCMC fitting. (Continued from Table 4)

ID	Model	$T_{\rm eff}$ (K)		log g (cgs)		Z ([M/H])		C/O		log K_{zz} (cgs)		D (pc)		Type
BD16	Sonora-Bobcat	$1\,320^{+48}_{-47}$	1 330	$5.2^{+0.3}_{-0.4}$	5.6	$-0.1^{+0.5}_{-0.3}$	−0.5					2224^{+447}_{-273}	2 082	Y0
	ATMO2020++	$1\,125^{+42}_{-32}$	1 104	$5.5^{+0.1}_{-0.1}$	5.6	$0.3^{+0.1}_{-0.1}$	0.4					$1\,806^{+136}_{-91}$	1 762	
	LOWZ[a]	948^{+75}_{-145}	975	$4.1^{+0.4}_{-0.3}$	4.0	$0.9^{+0.1}_{-0.2}$	1.1	$0.6^{+0.3}_{0.3}$	0.5	$3.4^{+3.0}_{3.0}$	0.9	$1\,353^{+235}_{-352}$	1 425	
BD17	Sonora-Bobcat	$1\,220^{+22}_{-26}$	1219	$5.4^{+0.1}_{-0.2}$	5.5	$-0.3^{+0.3}_{-0.2}$	−0.5					1244^{+111}_{-66}	1 238	T5
	ATMO2020++	$1\,015^{+24}_{-15}$	1 012	$5.5^{+0.1}_{-0.1}$	5.5	$0.3^{+0.1}_{-0.1}$	0.4					$1\,039^{+54}_{-23}$	1 030	
	LOWZ	$1\,032^{+148}_{-58}$	1 012	$4.9^{+0.2}_{-0.3}$	5.0	$0.6^{+0.5}_{-0.4}$	1.1	$0.4^{+0.3}_{0.3}$	0.2	$3.5^{+3.0}_{3.0}$	5.5	$1\,194^{+116}_{-131}$	1 272	
BD18	Sonora-Bobcat	704^{+8}_{-8}	702	$5.5^{+0.1}_{-0.2}$	5.5	$-0.5^{+0.1}_{-0.1}$	−0.5					330^{+18}_{-7}	328	T7
	ATMO2020++	650^{+5}_{-5}	649	$5.5^{+0.1}_{-0.1}$	5.5	$0.3^{+0.1}_{-0.1}$	0.4					341^{+3}_{-3}	342	
	LOWZ	654^{+26}_{-28}	656	$4.3^{+0.6}_{-0.6}$	4.4	$-0.8^{+0.2}_{-0.2}$	−0.8	$0.5^{+0.3}_{0.3}$	0.1	$2.7^{+3.0}_{3.0}$	−0.5	383^{+30}_{-36}	394	
BD19	Sonora-Bobcat	$1\,052^{+25}_{-27}$	1056	$4.2^{+0.4}_{-0.4}$	4.3	$-0.1^{+0.4}_{-0.3}$	−0.5					$1\,622^{+183}_{-241}$	1 748	T8
	ATMO2020++	957^{+68}_{-46}	931	$5.3^{+0.2}_{-0.3}$	5.5	$0.1^{+0.2}_{-0.2}$	0.4					1055^{+171}_{-102}	980	
	LOWZ	866^{+68}_{-106}	915	$3.7^{+0.5}_{-0.2}$	3.4	$-0.0^{+0.4}_{-0.3}$	−0.2	$0.6^{+0.3}_{0.3}$	0.8	$4.4^{+4.4}_{4.3}$	0.2	924^{+166}_{-235}	990	
BD20	Sonora-Bobcat	963^{+32}_{-32}	965	$4.9^{+0.4}_{-0.5}$	4.9	$-0.1^{+0.4}_{-0.3}$	−0.5					$1\,120^{+186}_{-143}$	1 048	T7
	ATMO2020++	847^{+20}_{-14}	848	$5.5^{+0.1}_{-0.1}$	5.5	$0.3^{+0.1}_{-0.1}$	0.3					870^{+31}_{-20}	866	
	LOWZ	857^{+59}_{-59}	850	$4.3^{+0.6}_{-0.5}$	4.2	$-0.2^{+0.3}_{-0.2}$	−0.2	$0.6^{+0.3}_{0.3}$	0.5	$2.7^{+3.2}_{3.0}$	−0.5	955^{+143}_{-135}	932	
BD21	Sonora-Bobcat	$1\,401^{+64}_{-65}$	1 412	$3.4^{+0.5}_{-0.4}$	3.0	$0.0^{+0.4}_{-0.4}$	−0.0					$4\,482^{+654}_{-614}$	4 428	T2
	ATMO2020++	$1\,189^{+15}_{-29}$	1 204	$4.2^{+0.3}_{-0.4}$	4.3	$0.1^{+0.2}_{-0.3}$	0.4					$2\,041^{+72}_{-101}$	2 072	
	LOWZ	$1\,396^{+94}_{-114}$	1 386	$4.0^{+0.7}_{-0.4}$	3.4	$-0.4^{+0.7}_{-0.9}$	−0.4	$0.5^{+0.3}_{0.3}$	0.5	$4.4^{+4.3}_{3.9}$	−0.5	$2\,916^{+317}_{-442}$	2 975	
BD22	Sonora-Bobcat	$1\,330^{+71}_{-66}$	1 338	$3.7^{+0.5}_{-0.4}$	3.6	$0.1^{+0.4}_{-0.4}$	0.5					$4\,160^{+730}_{-683}$	4 058	T5
	ATMO2020++	$1\,172^{+27}_{-48}$	1 200	$4.4^{+0.4}_{-0.6}$	4.6	$-0.1^{+0.4}_{-0.5}$	0.4					$2\,203^{+133}_{-189}$	2 298	
	LOWZ[a]	$1\,488^{+70}_{-81}$	1 510	$3.9^{+0.4}_{-0.3}$	3.6	$0.7^{+0.3}_{-0.5}$	1.1	$0.2^{+0.3}_{0.3}$	0.3	$5.3^{+4.0}_{4.6}$	7.5	$3\,217^{+331}_{-362}$	3 280	
BD23	Sonora-Bobcat	$1\,372^{+12}_{-10}$	1 369	$4.2^{+0.2}_{-0.2}$	4.2	$-0.1^{+0.1}_{-0.1}$	−0.1					$1\,588^{+106}_{-102}$	1 575	T2
	ATMO2020++	$1\,202^{+5}_{-6}$	1 201	$4.7^{+0.1}_{-0.1}$	4.7	$0.3^{+0.1}_{-0.1}$	0.3					919^{+4}_{-6}	920	
	LOWZ	$1\,388^{+124}_{-55}$	1 504	$4.1^{+0.4}_{-0.4}$	4.2	$-1.6^{+1.1}_{-0.7}$	−2.5	$0.3^{+0.4}_{0.3}$	0.1	$5.1^{+4.1}_{3.9}$	10.1	$1\,453^{+142}_{-135}$	1 588	
BD24	Sonora-Bobcat	$1\,323^{+8}_{-10}$	1 322	$4.0^{+0.1}_{-0.1}$	4.0	$-0.1^{+0.1}_{-0.1}$	−0.1					$1\,389^{+55}_{-58}$	1 390	T3
	ATMO2020++	$1\,168^{+18}_{-16}$	1 163	$4.6^{+0.1}_{-0.1}$	4.6	$0.3^{+0.1}_{-0.1}$	0.2					831^{+28}_{-24}	821	
	LOWZ[a]	$1\,306^{+25}_{-31}$	1 304	$4.0^{+0.4}_{-0.5}$	4.4	$-2.3^{+0.3}_{-0.2}$	−2.4	$0.3^{+0.3}_{0.3}$	0.2	$4.9^{+4.0}_{4.0}$	4.8	$1\,115^{+47}_{-42}$	1 125	
BD25	Sonora-Bobcat	$1\,635^{+25}_{-26}$	1 638	$5.4^{+0.2}_{-0.2}$	5.6	$-0.3^{+0.2}_{-0.2}$	−0.3					$2\,089^{+183}_{-144}$	1 975	T2
	ATMO2020++	$1\,204^{+5}_{-5}$	1 203	$5.1^{+0.1}_{-0.1}$	5.1	$0.3^{+0.1}_{-0.1}$	0.3					$1\,320^{+10}_{-11}$	1 318	
	LOWZ[a]	$1\,574^{+18}_{-27}$	1 580	$4.4^{+0.3}_{-0.4}$	4.6	$-1.9^{+0.2}_{-0.2}$	−1.9	$0.6^{+0.3}_{0.3}$	0.5	$2.2^{+3.0}_{3.0}$	0.2	$2\,407^{+61}_{-81}$	2 442	
BD26	Sonora-Bobcat	$1\,495^{+2}_{-1}$	1 494	$4.8^{+0.1}_{-0.1}$	4.8	$0.1^{+0.1}_{-0.1}$	0.1					$413.6^{+0.8}_{-0.4}$	412.2	T2
	ATMO2020++	$1\,200^{+4}_{-4}$	1 200	$4.9^{+0.1}_{-0.1}$	4.9	$0.3^{+0.1}_{-0.1}$	0.4					$267.4^{+0.13}_{-0.13}$	267.4	
	LOWZ	$1\,483^{+2}_{-2}$	1 484	$4.2^{+0.1}_{-0.1}$	4.2	$-1.2^{+0.1}_{-0.1}$	−1.2	$0.5^{+0.3}_{0.3}$	0.5	$3.3^{+3.0}_{3.0}$	5.5	$441.5^{+0.4}_{-0.9}$	441.5	
BD27	Sonora-Bobcat	$1\,316^{+3}_{-4}$	1 316	$4.4^{+0.1}_{-0.1}$	4.4	$-0.4^{+0.1}_{-0.1}$	−0.4					600^{+3}_{-2}	601	T4
	ATMO2020++	$1\,189^{+17}_{-4}$	1 186	$5.2^{+0.1}_{-0.1}$	5.2	$-0.0^{+0.1}_{-0.1}$	−0.0					478^{+14}_{-3}	476	
	LOWZ	$1\,136^{+3}_{-21}$	1 137	$4.4^{+0.1}_{-0.1}$	4.4	$0.2^{+0.1}_{-0.1}$	0.2	$0.5^{+0.3}_{0.3}$	0.5	$3.2^{+3.0}_{3.0}$	3.5	471^{+2}_{-16}	472	

• Based on the SED fitting results, we found 25 T-dwarf and 2 Y-dwarf candidates.

• The distances of these brown dwarf candidates range from 0.3 to 4 kpc, with an effective temperature range of 700–1 500 K.

• The observed cumulative number counts at kpc scales look consistent with those from the solar neighbourhood in Kirkpatrick et al. (2021). However, this is based on the small number statistics and needs to be confirmed with the larger survey data.

• The number densities we measured are $(2.0 \pm 0.9) \times 10^{-6}$pc^{-3} for 900–1 050 K dwarf, $(1.2 \pm 0.7) \times 10^{-6}$pc^{-3} for 1 050–1 200 K dwarf, and $(4.4 \pm 1.3) \times 10^{-6}$pc^{-3} for 1 200–1 350 K dwarf.

We discover distant and faint brown dwarfs that have never been seen before, which are located in the Galactic thick disk. By identifying more distant brown dwarfs, their characteristics and the low-mass part of the stellar mass function can be probed at greater distances. These brown dwarf candidates are exciting targets for the JWST NIRSpec spectroscopy. With NIRSpec's 1–5 μm spectra, the physical properties of these brown dwarf candidates can be probed more precisely.

https://doi.org/10.1017/pasa.2025.25 Published online by Cambridge University Press

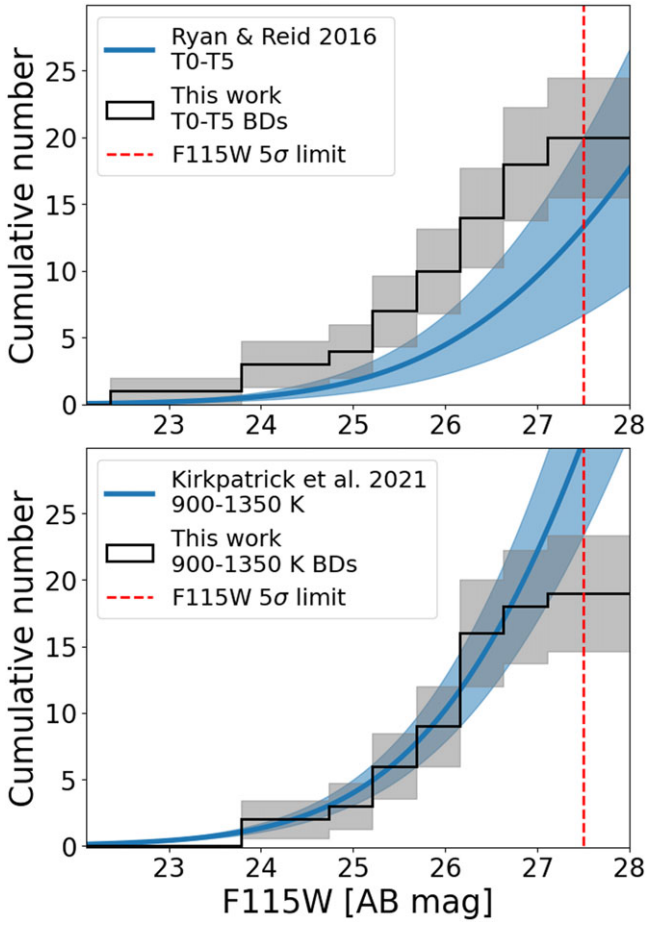


Figure 8. Cumulative number count against F115W magnitude. Upper panel: The black histogram shows the cumulative number count of T0–T5 candidates in this search. The grey region is one σ error assuming Poisson distribution. The blue curve is the model prediction from Ryan & Reid (2016). The red dashed line represents the 5σ detection limit of F115W. Lower panel: The black histogram is the cumulative number count of 900–1 350 K brown dwarf candidates in this search. These candidates are selected based on the peak $T_{\rm eff}$ value from Sonora-Bobcat's MCMC fitting results. The blue curve is the prediction scaled from Kirkpatrick et al. (2021)'s measurement. The red dashed line represents the 5σ detection limit of F115W.

Acknowledgement. We would like to express our deepest appreciation to the anonymous referee for the comprehensive and thoughtful review of our manuscript. Their detailed examination and insightful suggestions have played a crucial role in refining our work, and the constructive feedback has greatly enhanced the overall quality and clarity of the paper. AC acknowledges the Taiwan Astronomical ObserVatory Alliance (TAOvA) grant NSTC113-2740-M008-005 for the summer student internship in partial financial support of this research. TG acknowledges the support of the National Science and Technology Council of Taiwan through grants 108-2628-M-007-004-MY3, 110-2112-M-005-013-MY3, 111-2112-M-007-021, 111-2123-M-001-008-, 112-2112-M-007-013, 112-2123-M-001-004-, 113-2112-M-007-006 -, 113 -2927-I-007 -501 -, and 113-2123-M-001 -008 -. TH acknowledges the support of the National Science and Technology Council of Taiwan through grants 110-2112-M-005 -013 -MY3, 113-2112-M-005-009-MY3, 110-2112-M-007-034-, and 113-2123-M-001-008-. SH acknowledges the support of the Australian Research Council (ARC) Centre of Excellence (CoE) for Gravitational Wave Discovery (OzGrav) project numbers CE170100004 and CE230100016, and the ARC CoE for All Sky Astrophysics in 3 Dimensions (ASTRO 3D) project number CE170100013.

This research has made use of the SVO Filter Profile Service 'Carlos Rodrigo', funded by MCIN/AEI/10.13039/501100011033/ through grant PID2020-112949GB-I00. This work is based on observations made with the NASA/ESA/CSA James Webb Space Telescope. The data were obtained from the Mikulski Archive for Space Telescopes at the Space Telescope Science Institute, which is operated by the Association of Universities for Research in Astronomy, Inc., under NASA contract NAS 5-03127 for *JWST*. These observations are associated with the program ERO. This research has made use of the NASA/IPAC Infrared Science Archive, which is funded by the National Aeronautics and Space Administration and operated by the California Institute of Technology. This research has benefitted from the SpeX Prism Spectral Libraries, maintained by Adam Burgasser at http://www.browndwarfs.org/spexprism

This work used high-performance computing facilities operated by the Center for Informatics and Computation in Astronomy (CICA) at National Tsing Hua University. This equipment was funded by the Ministry of Education of Taiwan, the National Science and Technology Council of Taiwan, and the National Tsing Hua University.

Data availability statement. The JWST/NIRCam COSMOS-Web DR0.5 are publicly available at https://cosmos.astro.caltech.edu/page/cosmosweb-dr.

References

Allers, K. N., & Liu, M. C. 2013, AJ, 772, 79. https://doi.org/10.1088/0004-637X/772/2/79.

Arnouts, S., Cristiani, S., Moscardini, L., Matarrese, S., Lucchin, F., Fontana, A., & Giallongo, E. 1999, MNRAS, 310, 540. https://doi.org/10.1046/j.1365-8711.1999.02978.x. arXiv: astro-ph/9902290 [astro-ph].

Beiler, S. A., Mukherjee, S., Cushing, M. C., Davy Kirkpatrick, J., Schneider, A. C., Kothari, H., Marley, M. S., & Visscher, C. 2024, https://doi.org/10.48550/arXiv.2407.15950

Bertin, E., & Arnouts, S. 1996, A&AS, 117, 393. https://doi.org/10.1051/aas:1996164.

Bochanski, J. J., Hawley, S. L., Covey, K. R., West, A. A., Neill Reid, I., Golimowski, D. A., & Ivezic, Ž. 2010, AJ, 139, 2679. https://doi.org/10.1088/0004-6256/139/6/2679.

Bouy, H., Bertin, E., Moraux, E., Cuillandre, J.-C., Bouvier, J., Barrado, D., Solano, E., & Bayo, A. 2013, A&A, 554, A101. https://doi.org/10.1051/0004-6361/201220748.

Burgasser, A. J., et al. 2024, ApJ, 962, 177. https://doi.org/10.3847/1538-4357/ad206f.

Burgasser, A. J., Geballe, T. R., Leggett, S. K., Davy Kirkpatrick, J., & Golimowski, D. A. 2006, ApJ, 637, 1067. https://doi.org/10.1086/498563. arXiv: astro-ph/0510090 [astro-ph].

Bushouse, H., et al. 2023, https://doi.org/10.5281/zenodo.7795697.

Calzetti, D., Kinney, A. L., & Storchi-Bergmann, T. 1994, ApJ, 429, 582. https://doi.org/10.1086/174346.

Casey, C. M., et al. 2023, ApJ, 954, 31. https://doi.org/10.3847/1538-4357/acc2bc. arXiv: 2211.07865 [astro-ph.GA].

Chabrier, G., Baraffe, I., Allard, F., & Hauschildt, P. 2000, ApJ, 542, 464. https://doi.org/10.1086/309513. arXiv: astro-ph/0005557 [astro-ph].

Coleman, G. D., Wu, C.-C., & Weedman, D. W. 1980, ApJS, 43, 393. https://doi.org/10.1086/190674.

Cruz, K. L., et al. 2007. AJ, 133, 439. https://doi.org/10.1086/510132.

Cushing, M. C., et al. 2011, ApJ, 743, 50. https://doi.org/10.1088/0004-637X/743/1/50. arXiv: 1108.4678 [astro-ph.SR].

Franco, M., et al. 2023, arXiv e-prints (August): arXiv:2308.00751. https://doi.org/10.48550/arXiv.2308.00751.

Gardner, J. P., et al. 2023, PASP, 135, 068001. https://doi.org/10.1088/1538-3873/acd1b5.

Gardner, J. P., et al. 2006, SSR, 123, 485. https://doi.org/10.1007/s11214-006-8315-7.

Gizis, J. E., Allers, K. N., Liu, M. C., Harris, H. C., Faherty, J. K., Burgasser, A. J., & Davy Kirkpatrick, J. 2015, ApJ, 799, 203. https://doi.org/10.1088/0004-637X/799/2/203.

Hainline, K. N., et al. 2024a, ApJ, 975, 31. https://doi.org/10.3847/1538-4357/ad76a7.
Hainline, K. N., et al. 2024b, ApJ, 964, 66. https://doi.org/10.3847/1538-4357/ad20d1.
Hallakoun, N., & Maoz, D. 2021, MNRAS, 507, 398. issn: 0035-8711. https://doi.org/10.1093/mnras/stab2145.
Hamuy, M., Suntzeff, N. B., Heathcote, S. R., Walker, A. R., Gigoux, P., & Phillips, M. M. 1994, PASP, 106, 566. https://doi.org/10.1086/133417.
Ilbert, O., et al. 2006, A&A, 457, 841. https://doi.org/10.1051/0004-6361:20065138. arXiv: astro-ph/0603217 [astro-ph].
Kalirai, J. 2018, CoPh 59, 251. https://doi.org/10.1080/00107514.2018.1467648.
Kirkpatrick, J. D., et al. 2021, ApJS, 253, 7. https://doi.org/10.3847/1538-4365/abd107. arXiv: 2011.11616 [astro-ph.SR].
Kirkpatrick, J. D., et al. 1999, ApJ, 519, 802. https://doi.org/10.1086/307414.
Koekemoer, A. M., et al. 2007, ApJS, 172, 196. https://doi.org/10.1086/520086. arXiv: astro-ph/0703095 [astro-ph].
Langeroodi, D., & Hjorth, J. 2023, ApJ, 957, L27. https://doi.org/10.3847/2041-8213/acfeec. arXiv: 2308.10900 [astro-ph.GA].
Leggett, S. K., et al. 2021, ApJ, 918, 11. https://doi.org/10.3847/1538-4357/ac0cfe. arXiv: 2107.00696 [astro-ph.SR].
Lodieu, N., Zapatero Osorio, M. R., Martn, E. L., Rebolo López, R., & Gauza, B. 2022, A&A, 663, A84. https://doi.org/10.1051/0004-6361/202243516.
Marley, M. S., & Robinson, T. D. 2015, ARA&A, 53, 279. issn: 1545-4282. https://doi.org/https://doi.org/10.1146/annurev-astro-082214-122522.
Marley, M., Saumon, D., Morley, C., Fortney, J., Visscher, C., Freedman, R., & Lupu, R. 2021a, https://doi.org/10.5281/zenodo.5063476.
Marley, M. S., et al. 2021b, ApJ, 920, 85. https://doi.org/10.3847/1538-4357/ac141d.
Martin, E. C., et al. 2017, ApJ, 838, 73. https://doi.org/10.3847/1538-4357/aa6338.
Martn, E. L., Basri, G., Zapatero-Osorio, M. R., Rebolo, R., & Garca López, R. J. 1998, ApJ, 507, L41. https://doi.org/10.1086/311675.
Martn, E. L., Delfosse, X., Basri, G., Goldman, B., Forveille, T., & Zapatero Osorio, M. R. Z. 1999, AJ, 118, 2466. https://doi.org/10.1086/301107.
Martn, E. L., Zhang, J. -Y., Lanchas, H., Lodieu, N., Shahbaz, T., & Pavlenko, Ya. V. 2024, A&A, 686, A73. https://doi.org/10.1051/0004-6361/202347581. arXiv: 2403.12464 [astro-ph.SR].
McElwain, M. W., et al. 2023, PASP, 135, 058001. https://doi.org/10.1088/1538-3873/acada0.
Meisner, A. M., Leggett, S. K., Logsdon, S. E., Schneider, A. C., Tremblin, P., & Phillips, M. 2023, AJ, 166, 57. https://doi.org/10.3847/1538-3881/acdb68.
Meisner, A. M., et al. 2021, ApJ, 915, 120. https://doi.org/10.3847/1538-4357/ac013c.
Metchev, S. A., Davy Kirkpatrick, J., Bruce Berriman, G., & Looper, D. 2008, ApJ, 676, 1281. https://doi.org/10.1086/524721. arXiv: 0710.4157 [astro-ph].
Netzer, H., et al. 2007, ApJ, 666, 806. https://doi.org/10.1086/520716. arXiv: 0706.0818 [astro-ph].
Nonino, M., et al. 2023, ApJ, 942, L29. https://doi.org/10.3847/2041-8213/ac8e5f. arXiv: 2207.14802 [astro-ph.SR].
Osorio, M. R. Z., Béjar, V. J. S., Martn, E. L., Rebolo, R., Barrado y Navascués, D., Bailer-Jones, C. A. L., & Mundt, R. 2000, Sci, 290, 103. https://doi.org/10.1126/science.290.5489.103.
PeÑa Ramrez, K., Béjar, V. J. S., Zapatero Osorio, M. R., Petr-Gotzens, M. G., & Martn, E. L. 2012, ApJ, 754, 30. https://doi.org/10.1088/0004-637X/754/1/30.
Pickles, A. J. 1998, PASP, 110, 863. https://doi.org/10.1086/316197.
Rebolo, R., Martn, E. L., Basri, G., Marcy, G. W., & Zapatero-Osorio, M. R. 1996, ApJ, 469, L53. https://doi.org/10.1086/310263.
Rebolo, R., Zapatero Osorio, M. R., & Martn, E. L. 1995, Natur, 377, 129. https://doi.org/10.1038/377129a0.
Reid, I. N., Cruz, K. L., Davy Kirkpatrick, J., Allen, P. R., Mungall, F., Liebert, J., Lowrance, P., & Sweet, A. 2008, AJ, 136, 1290. https://doi.org/10.1088/0004-6256/136/3/1290.
Rieke, M. J., et al. 2023, PASP, 135, 028001. https://doi.org/10.1088/1538-3873/acac53. arXiv: 2212.12069 [astro-ph.IM].
Rowan-Robinson, M., et al. 2008, MNRAS, 386, 697. https://doi.org/10.1111/j.1365-2966.2008.13109.x. arXiv: 0802.1890 [astro-ph].
Ryan, Jr., R. E., & Reid, I. N. 2016, AJ, 151, 92. https://doi.org/10.3847/0004-6256/151/4/92. arXiv: 1510.05019 [astro-ph.GA].
Scoville, N., et al. 2007a, ApJS, 172, 38. https://doi.org/10.1086/516580.
Scoville, N., et al. 2007b, ApJS, 172, 1–8. https://doi.org/10.1086/516585.
Silva, L., Granato, G. L., Bressan, A., & Danese, L. 1998, ApJ, 509, 103. https://doi.org/10.1086/306476.
Taniguchi, Y., et al. 2015, PASJ, 67, 104. issn: 0004-6264. https://doi.org/10.1093/pasj/psv106. eprint: https://academic.oup.com/pasj/article-pdf/67/6/104/54683203/pasj_67_6_104.pdf. https://doi.org/10.1093/pasj/psv106.
Wang, P.-Y., et al. 2023, MNRAS, 523, 4534. issn: 0035-8711. https://doi.org/10.1093/mnras/stad1679.
Weaver, J. R., et al. 2022, ApJS, 258, 11. https://doi.org/10.3847/1538-4365/ac3078. arXiv: 2110.13923 [astro-ph.GA].
Yamamura, I., Tsuji, T., Tanabé, T., & Nakajima, T. 2009, in Akari, a Light to Illuminate the Misty Universe, Vol. 418, Astronomical Society of the Pacific Conference Series, ed. T. Onaka, G. J. White, T. Nakagawa, & I. Yamamura, 143.
Zhang, M., Xiang, M., Zhang, H.-W., Ting, Y.-S., Wu, Y.-Q., & Liu, X.-W. 2023, ApJ, 946, 110. https://doi.org/10.3847/1538-4357/acbcc4.

https://doi.org/10.1017/pasa.2025.25 Published online by Cambridge University Press